Title

Molecular Imaging with Aquaporin-Based Reporter Genes: Quantitative Considerations from Monte Carlo Diffusion Simulations

Journal

ACS Synthetic Biology, 12(10)

ISSN

2161-5063

Authors

Chowdhury, Rochishnu

Wan, Jinyang

Gardier, Remy

et al.

Publication Date

2023-10-20

DOI

10.1021/acssynbio.3c00372

Peer reviewed

HHS Public Access

Author manuscript

ACS Synth Biol. Author manuscript; available in PMC 2024 November 29.

Published in final edited form as:

ACS Synth Biol. 2023 October 20; 12(10): 3041–3049. doi:10.1021/acssynbio.3c00372.

Molecular imaging with aquaporin-based reporter genes: quantitative considerations from Monte Carlo diffusion simulations

Rochishnu Chowdhury[1], **Jinyang Wan**[2], **Remy Gardier**[7,#], **Jonathan Rafael-Patino**[7,8,#], **Jean-Philippe Thiran**[7,8], **Frederic Gibou**[1,9], **Arnab Mukherjee**[*,2,3,4,5,6]

[1]Department of Mechanical Engineering, University of California, Santa Barbara, CA 93106, USA

[2]Department of Chemistry, University of California, Santa Barbara, CA 93106, USA

[3]Department of Chemical Engineering, University of California, Santa Barbara, CA 93106, USA

[4]Biomolecular Science and Engineering, University of California, Santa Barbara, CA 93106, USA

[5]Biological Engineering, University of California, Santa Barbara, CA 93106, USA

[6]Neuroscience Research Institute, University of California, Santa Barbara, CA 93106, USA

[7]Signal Processing Laboratory (LTS5), Ecole Polytechnique Fédérale de Lausanne (EPFL), Lausanne, Switzerland

[8]Radiology Department, Centre Hospitalier Universitaire Vaudois (CHUV) and University of Lausanne (UNIL), Lausanne, Switzerland

[9]Department of Computer Science, University of California, Santa Barbara, CA 93106, USA

Abstract

Aquaporins provide a unique approach for imaging genetic activity in deep tissues by increasing the rate of cellular water diffusion, which generates magnetic resonance contrast. However, distinguishing aquaporin signals from the tissue background is challenging because water diffusion is influenced by structural factors such as cell size and packing density. Here, we developed a Monte Carlo model to analyze how cell radius and intracellular volume fraction quantitatively affect aquaporin signals. We demonstrated that a differential imaging approach

[*]Correspondence should be addressed to AM (arnabm@ucsb.edu).

[#]denotes equation contribution

Author Contributions

Rochishnu Chowdhury: Investigation, Validation, Formal analysis, Data Curation, Writing - Original Draft, Writing - Review & Editing. **Jinyang Wan**: Investigation, Validation, Formal analysis, Data Curation. **Remy Gardier**, **Jonathan Rafael-Patino, Jean-Philippe Thiran**: Methodology, Resources, Writing - Review & Editing. **Frederic Gibou**: Supervision, Funding acquisition, Writing - Review & Editing. **Arnab Mukherjee:** Conceptualization, Methodology, Formal analysis, Resources, Data Curation, Writing - Original Draft, Writing - Review & Editing, Visualization, Supervision, Project administration, Funding acquisition.

Supporting Information: The following files are available free of charge: “Chowdhury-Wan et al SI 2023”. The file contains supplementary figures S1–S6, depicting the experimental measurement of diffusivities in wild-type and Aqp1-expressing cells, dependence of diffusivity and SNR on diffusion time, effects of cell size and volume fraction on diffusivity, imaging of mixed-cell populations, representative workflow for generating synthetic mixed cell images from diffusion-weighted images, and simulated dependence of diffusivity on diffusion time in Jurkat cells.

Conflicts of Interest

There are no conflicts to declare.

based on subtracting signals at two diffusion times can improve specificity by unambiguously isolating aquaporin signals from the tissue background. We further used Monte Carlo simulations to analyze the connection between diffusivity and the percentage of cells engineered to express aquaporin, and established a mapping that accurately determined the volume fraction of aquaporin-expressing cells in mixed populations. The quantitative framework developed in this study will enable a broad range of applications in biomedical synthetic biology, requiring the use of aquaporins to noninvasively monitor the location and function of genetically engineered devices in live animals.

Graphical Abstract

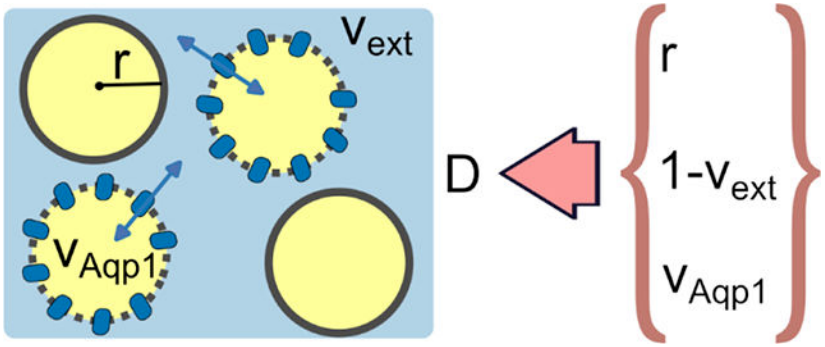

Keywords

MRI; aquaporins; reporter genes; Monte Carlo diffusion simulations; diffusion-weighted imaging; tissue microstructure

Introduction

Genetically encoded reporters are essential tools for monitoring molecular signals in living systems. In synthetic biology, reporters based on fluorescent and bioluminescent proteins provide a natural approach for measuring and optimizing the performance of genetic systems[1]. However, optical reporters are of limited use for tracking genetically engineered devices in living animals due to absorption and scattering of light in thick tissue[2–4]. Unlike optical methods, magnetic resonance imaging (MRI) can image deep tissues and generate volumetric scans with a high spatial resolution. We recently developed an MRI-based reporter that enables imaging of genetic activity in deep tissues[5,6]. This reporter utilizes aquaporin-1 (Aqp1), a channel consisting of a ~ 2.8 nm long and ~ 0.3 nm wide pore[7] that allows water molecules to diffuse freely albeit selectively across the plasma membrane[8,9]. In contrast to wild-type cells, which restrict water movement owing to the low permeability of the plasma membrane, cells engineered to express Aqp1 allow the free exchange of water (Fig. 1a). Accordingly, Aqp1 expression increases the molecular diffusivity of water in cells and tissues, which can be visualized using an MRI technique known as diffusion-weighted imaging[10,11]. In this technique, pulsed magnetic field gradients create a phase dispersion in water molecules, producing a signal that decays in proportion to water diffusivity.

Although Aqp1 provides a promising tool for monitoring genetic systems using MRI, variations in tissue microstructure, such as cell size and intracellular volume fraction, i.e., fraction of the total imaging volume occupied by cells, can affect tissue water diffusion[12–17], thereby making it difficult to unambiguously link Aqp1-driven signals with a specific genetic output or cell-type. For example, a decrease in intracellular volume fraction as a result of cell death or apoptotic shrinkage could lead to an increase in the rate of water diffusion in tissues independent of Aqp1 expression[18–20]. Conversely, an increase in cell size owing to swelling or mitotic growth arrest can decrease the rate of water diffusion[12,21,22]. To expand Aqp1 into a broadly useful reporter for biomedical applications of synthetic biology, we need a mechanistic framework that predicts how changes in molecular diffusivity induced by Aqp1 expression are affected by cell radius, packing density, and the volume fraction of Aqp1-expressing cells.

Monte Carlo diffusion simulations, which compute the Brownian motion of water molecules in the presence of a dephasing magnetic field gradient, are widely used to investigate the correlation between molecular diffusion of water and tissue morphology[23–37]. For example, Monte Carlo simulations have been used to quantify changes in white matter diffusivity caused by the swelling and beading of neurites during ischemic stroke[33,38]. In cancer biology, Monte Carlo methods have been used to explore the effects of cell size, packing density, and compartment volume fractions on tumor diffusion[27,32]. We recently applied Monte Carlo diffusion simulations to generate ground-truth diffusion datasets, which we used to compare the accuracies of various analytical models for estimating tissue microstructure using diffusion-weighted MRI[36].

In this study, we developed and experimentally validated a Monte Carlo simulator to model water diffusion in cells engineered to express Aqp1. We showed that Aqp1 operates as an effective reporter over a wide range of cell sizes and volume fractions, driving larger changes in molecular diffusivity than those seen in wild-type (viz. non-engineered) cells. We also identified the range of cellular radii and volume fractions that lead to nonspecific enhancements in molecular diffusivity, thereby making it nontrivial to unambiguously discern Aqp1-based MRI signals from the tissue background. We further show that by subtracting diffusion coefficients obtained at two diffusion times, Aqp1-expression can be specifically detected without interference from the background. Finally, we used Monte Carlo simulations to analyze the correlation between diffusivity and the volume fraction of Aqp1-expressing cells and demonstrated that a simple log-linear model was sufficient to measure Aqp1-expressing cells in mixed-cell populations, thereby combining cell-type specificity with quantitative imaging.

Results

Aqp1 generates a substantial increase in diffusivity at long diffusion times

We designed our computational tissue phantom to consist of spherical cells (7.6 μm radius) tightly packed to yield an intracellular volume fraction of 0.65. This configuration mimics our experimental system comprising lightly centrifuged pellets of Chinese hamster ovary (CHO) cells. We used Monte Carlo simulations to compute diffusivities for a range of permeability coefficients and diffusion times. Consistent with previous studies of water

diffusion in similar geometries[39], the diffusivity increases with membrane permeability, rising sharply as the permeability crosses ~10^{-2} $\mu m/ms$ (Fig. 1b). Longer diffusion times lead to a decrease in diffusivity as more spins encounter the plasma membrane, which restricts water movement (Fig. 1b,c). In contrast, permeable membranes (e.g., due to Aqp1 expression) do not substantially hinder the free movement of water molecules and thus the time dependence of diffusion become less pronounced with increasing permeability (Fig. 1c). Accordingly, extended diffusion times are optimal for maximizing diffusion-weighted contrast induced by Aqp1 expression.

Next, we used diffusion-weighted MRI to measure diffusivities in pellets of both wild-type cells and cells in which the Aqp1 reporter was introduced as a transgene using lentiviral transduction (Supplementary Fig. 1). Our experimental estimates agreed with diffusion coefficients computed from Monte Carlo simulations where we modeled wild-type and Aqp1-CHO cells using permeability coefficients of 0.012 and 0.138 $\mu m/ms$ respectively based on previously published estimates[40,41] (Fig. 1c). Notably, at a diffusion time of 100 ms, Aqp1-expressing cells showed a 124 $\pm$ 14 % (mean ± s.d., $n = 6$) increase in diffusivity compared to wild-type cells, which aligns well with the 112 % increase predicted from our simulations. Longer diffusion times will further enhance the Aqp1-driven increase in diffusivity (Supplementary Fig. 2a), though this also sharply decreases the signal-to-noise ratio (SNR) in diffusion-weighted images (Supplementary Fig. 2b). Accordingly, in the remainder of the study, we use 100 ms as our long diffusion time limit to achieve an optimal trade-off between diffusion fold-change and SNR.

Changes in tissue microstructure may elevate diffusion rates, at times overlapping with Aqp1-driven changes in molecular diffusivity

We applied the Monte Carlo diffusion framework to explore the effects of tissue microstructure parameters, namely cell size (r) and intracellular volume fraction (v_f) on the diffusivities of wild-type and Aqp1-expressing CHO cells. We varied cellular radii from 5 to 25 μm to represent both small (e.g., monocytes[42]) and large cell-types (e.g., adipocytes). We set the upper bound of the intracellular volume fraction as 0.67, which corresponds to typical packing of cells in pellets and many tissues[33,43]. For the lower bound on v_f, we used a value of 0.1 to represent conditions where the intracellular volume is substantially reduced by edema or necrosis, for example during tumor therapy[44,45]. Our specific goal was to identify cell sizes and volume fractions that would elevate the rate of water diffusion and by doing so create the same effect on MRI readouts as the Aqp1 reporter (Fig. 2a). In practical terms, this parameter space represents tissue configurations where Aqp1 signals are hard to tell apart from the tissue background. For a fixed intracellular volume fraction, we found that wild-type diffusivity was highly sensitive to cell size, increasing by as much as 122 % as the radius was varied from 5 μm to 25 μm (Fig. 2b). Expression of Aqp1 reduced the cell size dependence, producing a 36 % increase in diffusivity over the same size range (Fig. 2b). Wild-type cells were also more sensitive to changes in the intracellular volume fraction and their diffusivity increased by 177 % (compared to 80 % for Aqp1 cells) when the volume fraction was increased over a 5-fold range, while keeping the cell radius fixed (Fig. 2c).

Next, we calculated diffusivities while simultaneously varying both the intracellular volume fraction and cell size (Fig. 2d,e). The maximum fold-change in diffusivity of Aqp1-expressing cells compared to wild-type cells occurs in the $5 - 7\ \mu m$ cell radius range and for volume fractions greater than 0.65. Importantly, configurations comprising large cells and low intracellular volume fractions had diffusivities high enough to overlap with Aqp1 signals (Fig. 2d,e). Accordingly, we wondered whether we could use the distinct time-dependence of diffusivity in wild-type and Aqp1-expressing cells (Fig. 1c) to unambiguously locate Aqp1-based signals in the parameter space where Aqp1-driven diffusivity changes are masked by elevations in background tissue diffusion. Notably, in sharp contrast to Aqp1-expressing cells, the diffusivity of wild-type cells changes rapidly with diffusion time (Fig. 1c). Accordingly, we explored how the difference in simulated diffusivities between $20\ ms$ and $100\ ms$ ($\Delta D = D_{20} - D_{100}$) changes as a function of radii and intracellular volume fractions (Fig. 2f,g, Supplementary Fig. 3). Strikingly, the ΔD metric successfully differentiated between wild-type and Aqp1-expressing cells for nearly all combinations of radii and volume fractions tested (Fig. 2f), indicating that difference imaging at two diffusion times provides a unique approach for accurately identifying expression of the Aqp1 reporter regardless of changes in microstructure parameters.

Monte Carlo simulations allow mapping of Aqp1 volume fraction in mixed cell populations

In many applications of reporter gene technology, such as tracking cell therapies and monitoring transcriptional activity, only a subset of cells may express the reporter at a given time. In these scenarios, the ability to quantify the fraction of reporter-expressing cells permits a richer description of the underlying biological process. To this end, we hypothesized that the dependence of molecular diffusivity on the volume fraction of Aqp1- cells (v_{Aqp1}) in a mixed population could be used for quantitative imaging of reporter gene expression (Fig. 3a). To test this idea, we analyzed the relationship between diffusivity calculated by our Monte Carlo simulations and v_{Aqp1} in mixed populations comprising CHO-Aqp1 cells interspersed with wild-type cells in varying ratios. We found that a simple log-linear function quantitatively describes the dependence of molecular diffusivity on v_{Aqp1} (Fig. 3b, Supplementary Fig. 4). Next, we constructed a mixed-cell mosaic by randomly sampling pixels from experimental diffusion maps of cell populations comprising varying ratios of Aqp1-expressing to wild-type CHO cells (Supplementary Fig. 5, Fig. 3c). We used the log-linear mapping between diffusivity and v_{Aqp1} (Fig. 3b) to classify each pixel in the mosaic into one of four groups mirroring the percentage of Aqp1-labeled cells contained in the pixel (Fig. 3d). Using this approach, we were able to convert the mixed-cell image into a 4-level classification of Aqp1 volume fraction achieving an accuracy of 79.67 % on entirely unseen experimental data (Fig. 3e, Table 1). We further tested this approach on a cell mixture consisting of CHO-Aqp1 cells mixed with a different cell-type, Jurkat T-cells. We simulated Jurkat cells as spheres with a radius of $5\ \mu m$ and validated that the simulated diffusivity matched with experimental measurements in cell pellets (Supplementary Fig. 6). As before, we generated mixed-cell mosaics from diffusion maps of pellets comprising CHO-Aqp1 cells mixed with Jurkat cells in varying ratios (Fig. 3f). Finally, we used the log-linear mapping between simulated diffusivity and v_{Aqp1} for the CHO-Aqp1 and Jurkat

mixture (Fig. 3b) to perform a 4-level classification of all pixels in the mosaic image, achieving an accuracy of 78.15 % (Fig. 3g,h, Table 2).

Discussion

Here, we quantitatively assessed the performance of Aqp1 as a reporter gene in simulated tissue configurations comprising cells of different radii, volume fractions, and proportions of Aqp1-expressing cells. Our study revealed four major findings that we anticipate will be used to guide the design and analysis of future experiments involving Aqp1 to track cells, genetic function, and molecular signals in living organisms. First, we found that Aqp1 is robust to cell size variations, making it a suitable reporter for cells of different sizes. This prediction is reinforced by a growing body of literature showing that Aqp1 operates as a viable reporter across distinct cell-types, such as tumors, neurons, and glial cells[46–48]. Second, this study emphasizes the importance of accounting for volume fraction when interpreting MRI signals generated by Aqp1, especially when a large reduction in cell density is expected, such as during tumor therapy. Third, we demonstrate that subtracting diffusivities at short ($20\ ms$) and long diffusion times ($100\ ms$) provides a unique approach for disambiguating Aqp1 signals from the nonspecific effects of tissue microstructure on water diffusion. With continued technical advances that increase the SNR, for example, higher-field magnets (18 T is now commercially available for preclinical imaging), cryogenically cooled coils, and machine learning-based SNR recovery techniques, the long time limit can be further extended beyond 100 ms, which would further improve the separation between Aqp1-expressing cells and the background. Finally, we observed that diffusivity was quantitatively linked to the volume fraction of cells expressing Aqp1, suggesting that Aqp1 can be used as a genetic indicator to measure transcriptional activity or the percentage of reporter-expressing cells in mixed populations.

The current study has limitations, which suggest potential avenues for future research. First, the two-compartment model employed here, similar to those used in past diffusion modeling studies[26,31,34,39], could be amended to include additional water pools for subcellular structures such as the nucleus and extracellular structures such as the vasculature[27,32,49]. Such multicompartment models could help in analyzing how Aqp1 behaves in systems where nuclear and/or vascular volume fractions vary, which could in turn modify intra- and extracellular diffusion coefficients. Our framework can also be readily adapted to incorporate varying levels of Aqp1 expression achieved in different cell types or transgene expression systems by selecting an appropriate radius and permeability coefficient, which are easily measured experimentally. Second, our tissue phantoms can be tailored to accurately reflect realistic geometries derived from the histology of engineered tissues expressing Aqp1[50]. Although we expect that the correlations found in this study will hold for even more complex tissue morphologies, histology-derived meshes can be useful for exploring the context-dependent behavior of Aqp1 in realistic in vivo settings. To this end, Monte Carlo diffusion simulations have the advantage of easily integrating new experimental data, which is expected to grow as diffusion MRI technology continues to push the boundaries of sensitivity and resolution[51] and Aqp1-based reporters are more broadly adopted by the scientific community. Finally, Monte Carlo simulations could be used to train learning algorithms to generate spatial maps of gene expression and cell density based on

Aqp1 reporter signals measured in biological tissues[50]. To do so, the diffusion signal must be represented by a more comprehensive feature vector, likely including additional metrics derived from multishell diffusion-weighted imaging experiments[52]. These efforts should be bolstered by machine learning models that use multi-shell diffusion tensor data to compute tissue microstructure parameters[53–56].

In summary, this study presents a quantitative framework to analyze Aqp1 in a variety of tissue settings and lays the foundation for integrating Aqp1 with computational modeling to accurately locate and map spatiotemporal profiles of gene expression and cell-based devices in vertebrates.

Methods

Monte Carlo diffusion simulations

We modeled cells as packed spheres and dispersed $N = 10^5$ particles (representing diffusing water spins) evenly in the intra- and extracellular compartments, in proportion to the relative volume of each compartment. We performed two-compartment diffusion simulations with a time step (τ) of 19.682 μs using the open-source Monte Carlo Diffusion and Collision Simulator developed in[26] and later extended to permeable substrates[36]. The total number ofparticles (N) and step size (τ) were chosen to ensure accuracy and convergence of the simulation runs[26]. Using these parameters, the standard deviation of simulated diffusivity is less than 2 % of its mean across all simulations. Briefly, at each time step ($\tau = 19\ \mu s$), we randomly displaced a spin (i) by a distance (x_i) computed from Einstein's diffusion equation assuming diffusion coefficients of 1 μm^2/ms and 2 μm^2/ms for the intra- and extracellular compartments, respectively. Upon encountering the cell membrane, a water molecule can undergo an elastic reflection[25] or pass through the membrane with a probability that depends on the permeability coefficient (κ), which quantifies the rate of water permeation through the cell membrane[57]. The relation between this probability and κ is is calculated as described in prior work[50]. At the desired diffusion time (Δ), we sum the total phase dispersion of by all spins in the ensemble to compute the diffusion coefficient (D) as follows: $D = -\frac{\ln\left(e^{-\frac{q}{2}\sum x_i^2}\right)}{q\,\Delta}$. Here, q represents the diffusion-weighting defined as $q = (\gamma g \delta)^2$ where $\gamma = 42.57\ MHz/T$, δ is the gradient duration, g is the gradient strength. The values of Δ, δ, and g were based on the experimentally defined diffusion-weighted MRI parameters (see below). We first investigated the change in diffusivity as a function of membrane permeability for a fixed cell radius ($r = 7.6\ \mu m$) and volume fraction ($v_f = 0.65$). This radius was chosen to be consistent with the effective size of CHO cells[58] and the volume fraction approximates lightly centrifuged cell pellets as well as many physiological tissues. We investigated three scenarios: (1) $v_f = 0.65$, $5\ \mu m \leq r \leq 25\ \mu m$ (2) $r = 7.6\ \mu m$, $0.10 \leq v_f \leq 0.67$ (3) concurrently varying both r and v_f within the aforementioned limits. For each condition, we tested two permeability coefficients corresponding to wild-type ($0.012\ \mu m\ ms^{-1}$) and Aqp1-expressing CHO cells

($0.138\ \mu m\ ms^{-1}$). The permeability values are based on previously published estimates obtained in wild-type CHO cells and CHO cells stably transfected to express Aqp1[40].

Mixed-cell Monte Carlo simulations were performed in the same manner as described above, but by varying the number of Aqp1-expressing and wild-type CHO cells to achieve a desired Aqp1 volume fraction ($v_{f,\,Aqp1}$). For mixed-cell experiments involving CHO and Jurkat cells, the latter were modeled as smaller spheres ($r = 5\ \mu m$) with $\kappa = 0.005\ \mu m/ms$[59,60]. We packed spheres of two different radii ($r_{CHO} = 7.6\ \mu m$, $r_{Jurkat} = 5\ \mu m$) to obtain a total intracellular volume fraction of 0.65, as described previously[61], while adjusting the number of bigger spheres to obtain the desired volume fraction of CHO cells.

Reagents

Dulbecco's Modified Eagle Media (DMEM), sodium pyruvate, doxycycline hyclate, and penicillin-streptomycin (10^4 units/mL penicillin and 10 mg/mL streptomycin) were purchased from Sigma-Aldrich (St. Louis, MO, USA). Roswell Park Memorial Institute media (RPMI 1640), sterile phosphate buffered saline (PBS), TrypLE, and Gibco™ fetal bovine serum (FBS) were purchased from Thermo Fisher Scientific (Waltham, MA, USA). MycoAlert® Plus Mycoplasma Detection Assay was purchased from Lonza.

Cell culture

Chinese hamster ovary (CHO) cell lines were genetically engineered to express human aquaporin-1 (hAqp1) exactly as described in our previous work. Both wild-type and Aqp1-expressing CHO cells were cultured at 37 °C in a humidified 5 % CO_2 incubator using DMEM supplemented with 10 % FBS, 100 U/mL penicillin, and 100 μg/mL streptomycin. Jurkat cells were grown as suspension culture using RPMI medium supplemented as before.

In vitro MRI

Approximately 24 h before imaging, cells were treated with doxycycline hyclate (1–10 μg/mL) to activate Aqp1 expression. Adherent CHO cells were harvested by trypsinization, centrifuged at 350 x g, and resuspended in 200 μL sterile PBS in 0.2 mL tubes. For the mixed cell experiments, the two cell types were cultured separately and 10 μL of the cell suspension was loaded in a disposable hemocytometer to count cells using a bright field microscope. Based on the cell counts, appropriate volumes of the two cell types were mixed to achieve a desired volume fraction of Aqp1-expressing cells. The cells were mixed by gentle pipetting, centrifuged, and transferred to 0.2 mL tubes. The 0.2 mL tubes were centrifuged at a low speed (500 x g for 5 min) to form compact pellets. The pellet-containing tubes were housed in a water-filled agarose (1 % w/v) phantom for imaging. MR images were acquired using a 66 mm diameter coil in a Bruker 7T vertical-bore scanner. Diffusion-weighted images were acquired in the axial plane using a stimulated echo sequence with the following parameters: echo time, T_E = 18 ms, repetition time, T_R = 1000 ms, gradient duration, δ = 5 ms, gradient separation, Δ = 20, 50, 80, 100, 200, and 300 ms, matrix size = 128 × 128, field of view (FOV) = 5.08 × 5.08 cm^2, slice thickness = 1–2 mm, number of averages = 5, and 4 nominal b-values: 0, 400, 600, and 800 s/mm^2. The b-value determines the extent of diffusion-weighting applied to the polarized water molecules and is classically

defined as $b = (\gamma\delta G)^2\left(\Delta - \frac{\delta}{3}\right)$, where $\gamma = 42.57\ MHz\ T^{-1}$ is the proton gyromagnetic ratio and G is the magnitude of the gradient pulse. Although the same set of nominal b-values was used at all diffusion times, the effective b-values changed substantially owing to the contribution of imaging gradients to the diffusion weighting via cross terms[62]. Typically, the effective b-values in our MRI scanner rang from $46 - 2900\ s\ mm^{-2}$ for Δ values from $20\ to\ 300\ ms$.

Diffusion-weighted intensity was determined using region of interest (ROI) analysis in Fiji (NIH) and the slope of the logarithmic decay in mean intensity versus effective b-value was used to calculate the diffusivity. To generate pixel-wise diffusion maps, a diffusion coefficient was computed for each pixel. Least-squares regression fitting was performed in Matlab (R2022b) or Python v3.9.

Pixel-wise classification of mixed-cell populations based on Aqp1 volume fraction

We binned individual pixels from experimental diffusion maps (acquired at Δ = 100 ms) of mixed-cell pellets into one of nine groups (0, 10, 20, 30, 40, 50, 60, 80, and 100 %) based on the known Aqp1 volume fraction (v_{Aqp1}) of the pellet. The ensuing dataset comprises approximately 3744 pixels (4 replicates x 104 pixels per image x 9 v_{Aqp1} values) representing noisy experimental data for a range of Aqp1 volume fractions. We denoised diffusivity values in each bin using a Gaussian filter ($\sigma = 3$), similar to how experimental diffusion maps are commonly smoothed. From each bin, we sampled 64 pixels with replacement and distributed them randomly in a 24 × 24 grid to construct a “mixed-cell” ADC image. We modeled the dependence of the simulated ADC (Δ = 100 ms) on v_{Aqp1} using a log-linear function of the form $log(ADC) = av_{Aqp1} + b$. We used the resulting log-linear mapping to classify each pixel in the mixed-cell ADC image into one of four levels: absent ($v_{Aqp1} < 10\ \%$), low ($10\ \% \leq v_{Aqp1} < 30\ \%$), medium ($30\ \% \leq v_{Aqp1} \leq 70\ \%$), and high ($v_{Aqp1} > 70\ \%$). This discretized 4-level classification was deemed appropriate, given that experimental ADC maps are inherently noisy, particularly at the long diffusion times needed to maximize Aqp1-based contrast. To evaluate the performance of the model, we repeated the 4-level classification on 100 randomly generated sets of mixed-cell images and computed the confusion matrix using the precision_recall_fscore_support package from sklearn.metrics in Python.

Statistical analysis

Experimental data are summarized by their mean and standard deviation obtained from multiple ($n \geq 4$) biological replicates defined as measurements performed with distinct cell samples. Quality of model-fitting was judged based on the regression coefficient and inspection of the 95 % confidence intervals and coefficients of determination. All tests are 2-sided and a P value of less than 0.05 taken to indicate statistical significance.

Supplementary Material

Refer to Web version on PubMed Central for supplementary material.

Acknowledgements

We thank Dr. Harun F. Ozbakir, Dr. Jason Yun, and Dr. Thomas Oerther (Bruker BioSpin GmbH) for several helpful discussions and optimization of imaging protocols. This research was supported by the National Institutes of Health (R35-GM133530, R03-DA050971, and R01-NS128278 to A.M.), the U.S. Army Research Office via the Institute for Collaborative Biotechnologies cooperative agreement W911NF-19-D-0001-0009 (A.M.), a NARSAD Young Investigator Award from the Brain & Behavior Research Foundation (A.M.), and a UC Santa Barbara Office of Research Early-Stage Seed Grants (A.M. and F.G). This project has also been made possible in part by a grant from the Chan Zuckerberg Initiative DAF, an advised fund of Silicon Valley Community Foundation. All MRI experiments were performed at the Materials Research Laboratory (MRL) at UC, Santa Barbara. The MRL Shared Experimental Facilities are supported by the MRSEC Program of the NSF under Award No. DMR 1720256; a member of the NSF-funded Materials Research Facilities Network. We acknowledge the use of the NRI-MCDB Microscopy Facility and the Resonant Scanning Confocal supported by NSF MRI grant 1625770.

References

(1). Gilad AA; Shapiro MG Molecular Imaging in Synthetic Biology, and Synthetic Biology in Molecular Imaging. Mol Imaging Biol 2017, 19 (3), 373–378. 10.1007/s11307-017-1062-1. [PubMed: 28213833]

(2). Schuerle S; Furubayashi M; Soleimany AP; Gwisai T; Huang W; Voigt C; Bhatia SN Genetic Encoding of Targeted Magnetic Resonance Imaging Contrast Agents for Tumor Imaging. ACS Synth. Biol 2020, 9 (2), 392–401. 10.1021/acssynbio.9b00416. [PubMed: 31922737]

(3). Bricco AR; Miralavy I; Bo S; Perlman O; Korenchan DE; Farrar CT; McMahon MT; Banzhaf W; Gilad AA A Genetic Programming Approach to Engineering MRI Reporter Genes. ACS Synth. Biol 2023, 12 (4), 1154–1163. 10.1021/acssynbio.2c00648. [PubMed: 36947694]

(4). Helmchen F; Denk W. Deep Tissue Two-Photon Microscopy. Nat Methods 2005, 2 (12), 932–940. 10.1038/nmeth818. [PubMed: 16299478]

(5). Mukherjee A; Davis HC; Ramesh P; Lu GJ; Shapiro MG Biomolecular MRI Reporters: Evolution of New Mechanisms. Progress in Nuclear Magnetic Resonance Spectroscopy 2017, 102–103, 32–42. 10.1016/j.pnmrs.2017.05.002.

(6). Mukherjee A; Wu D; Davis HC; Shapiro MG Non-Invasive Imaging Using Reporter Genes Altering Cellular Water Permeability. Nat Commun 2016, 7 (1), 13891. 10.1038/ncomms13891. [PubMed: 28008959]

(7). Sui H; Han B-G; Lee JK; Walian P; Jap BK Structural Basis of Water-Specific Transport through the AQP1 Water Channel. Nature 2001, 414 (6866), 872–878. 10.1038/414872a. [PubMed: 11780053]

(8). Benga G. The First Discovered Water Channel Protein, Later Called Aquaporin 1: Molecular Characteristics, Functions and Medical Implications. Molecular Aspects of Medicine 2012, 33 (5), 518–534. 10.1016/j.mam.2012.06.001. [PubMed: 22705445]

(9). Verkman AS; Mitra AK Structure and Function of Aquaporin Water Channels. American Journal of Physiology-Renal Physiology 2000, 278 (1), F13–F28. 10.1152/ajprenal.2000.278.1.F13. [PubMed: 10644652]

(10). Bammer R. Basic Principles of Diffusion-Weighted Imaging. European Journal of Radiology 2003, 45 (3), 169–184. 10.1016/S0720-048X(02)00303-0. [PubMed: 12595101]

(11). Merboldt K-D; Hanicke W; Frahm J. Self-Diffusion NMR Imaging Using Stimulated Echoes. Journal of Magnetic Resonance (1969) 1985, 64 (3), 479–486. 10.1016/0022-2364(85)90111-8.

(12). Harkins KD; Galons J-P; Secomb TW; Trouard TP Assessment of the Effects of Cellular Tissue Properties on ADC Measurements by Numerical Simulation of Water Diffusion. Magnetic Resonance in Medicine 2009, 62 (6), 1414–1422. 10.1002/mrm.22155. [PubMed: 19785014]

(13). Xu J; Does MD; Gore JC Quantitative Characterization of Tissue Microstructure with Temporal Diffusion Spectroscopy. Journal of Magnetic Resonance 2009, 200 (2), 189–197. 10.1016/j.jmr.2009.06.022. [PubMed: 19616979]

(14). Bihan DL Molecular Diffusion, Tissue Microdynamics and Microstructure. NMR in Biomedicine 1995, 8 (7), 375–386. 10.1002/nbm.1940080711. [PubMed: 8739274]

(15). Nilsson M; van Westen D; Ståhlberg F; Sundgren PC; Lätt J. The Role of Tissue Microstructure and Water Exchange in Biophysical Modelling of Diffusion in White Matter. Magn Reson Mater Phy 2013, 26 (4), 345–370. 10.1007/s10334-013-0371-x.

(16). Pilatus U; Shim H; Artemov D; Davis D; van Zijl PC; Glickson JD Intracellular Volume and Apparent Diffusion Constants of Perfused Cancer Cell Cultures, as Measured by NMR. Magn Reson Med 1997, 37 (6), 825–832. 10.1002/mrm.1910370605. [PubMed: 9178232]

(17). Norris DG The Effects of Microscopic Tissue Parameters on the Diffusion Weighted Magnetic Resonance Imaging Experiment. NMR Biomed 2001, 14 (2), 77–93. 10.1002/nbm.682. [PubMed: 11320535]

(18). Galons J-P; Altbach MI; Paine-Murrieta GD; Taylor CW; Gillies RJ Early Increases in Breast Tumor Xenograft Water Mobility in Response to Paclitaxel Therapy Detected by Non-Invasive Diffusion Magnetic Resonance Imaging. Neoplasia 1999, 1 (2), 113–117. [PubMed: 10933044]

(19). Anderson NT; Weyant KB; Mukherjee A. Characterization of Flavin Binding in Oxygen-Independent Fluorescent Reporters. AIChE Journal 2020, 66 (12), e17083. 10.1002/aic.17083.

(20). Moffat BA; Chenevert TL; Lawrence TS; Meyer CR; Johnson TD; Dong Q; Tsien C; Mukherji S; Quint DJ; Gebarski SS; Robertson PL; Junck LR; Rehemtulla A; Ross BD Functional Diffusion Map: A Noninvasive MRI Biomarker for Early Stratification of Clinical Brain Tumor Response. Proc Natl Acad Sci U S A 2005, 102 (15), 5524–5529. 10.1073/pnas.0501532102. [PubMed: 15805192]

(21). Jiang X; Li H; Zhao P; Xie J; Khabele D; Xu J; Gore JC Early Detection of Treatment-Induced Mitotic Arrest Using Temporal Diffusion Magnetic Resonance Spectroscopy. Neoplasia 2016, 18 (6), 387–397. 10.1016/j.neo.2016.04.006. [PubMed: 27292027]

(22). Moseley ME; Cohen Y; Mintorovitch J; Chileuitt L; Shimizu H; Kucharczyk J; Wendland MF; Weinstein PR Early Detection of Regional Cerebral Ischemia in Cats: Comparison of Diffusion- and T2-Weighted MRI and Spectroscopy. Magnetic Resonance in Medicine 1990, 14 (2), 330–346. 10.1002/mrm.1910140218. [PubMed: 2345513]

(23). Fieremans E; Novikov DS; Jensen JH; Helpern JA Monte Carlo study of a two-compartment exchange model of diffusion. NMR in Biomedicine 2010, 23 (7), 711–724. 10.1002/nbm.1577. [PubMed: 20882537]

(24). Yeh C-H; Schmitt B; Bihan DL; Li-Schlittgen J-R; Lin C-P; Poupon C. Diffusion Microscopist Simulator: A General Monte Carlo Simulation System for Diffusion Magnetic Resonance Imaging. PLOS ONE 2013, 8 (10), e76626. 10.1371/journal.pone.0076626.

(25). Szafer A; Zhong J; Gore JC Theoretical Model for Water Diffusion in Tissues. Magnetic Resonance in Medicine 1995, 33 (5), 697–712. 10.1002/mrm.1910330516. [PubMed: 7596275]

(26). Rafael-Patino J; Romascano D; Ramirez-Manzanares A; Canales-Rodríguez EJ; Girard G; Thiran J-P Robust Monte-Carlo Simulations in Diffusion-MRI: Effect of the Substrate Complexity and Parameter Choice on the Reproducibility of Results. Front Neuroinform 2020, 14, 8. 10.3389/fninf.2020.00008. [PubMed: 32210781]

(27). Gilani N; Malcolm P; Johnson G. An Improved Model for Prostate Diffusion Incorporating the Results of Monte Carlo Simulations of Diffusion in the Cellular Compartment. NMR in Biomedicine 2017, 30 (12), e3782. 10.1002/nbm.3782.

(28). Gilani N; Malcolm P; Johnson G. A Monte Carlo Study of Restricted Diffusion: Implications for Diffusion MRI of Prostate Cancer: A Monte Carlo Study of Restricted Diffusion: Implications for Diffusion MRI of Prostate Cancer. Magn. Reson. Med 2017, 77 (4), 1671–1677. 10.1002/mrm.26230. [PubMed: 27059769]

(29). Hall MG; Alexander DC Convergence and Parameter Choice for Monte-Carlo Simulations of Diffusion MRI. IEEE Trans Med Imaging 2009, 28 (9), 1354–1364. 10.1109/TMI.2009.2015756. [PubMed: 19273001]

(30). Karunanithy G; Wheeler RJ; Tear L; Farrer NJ; Faulkner S; Baldwin AJ INDIANA: An in-Cell Diffusion Method to Characterize the Size, Abundance and Permeability of Cells. J Magn Reson 2019, 302, 1–13. 10.1016/j.jmr.2018.12.001. [PubMed: 30904779]

(31). Lee C-Y; Bennett KM; Debbins JP Sensitivities of Statistical Distribution Model and Diffusion Kurtosis Model in Varying Microstructural Environments: A Monte Carlo Study. Journal of Magnetic Resonance 2013, 230, 19–26. 10.1016/j.jmr.2013.01.014. [PubMed: 23428968]

(32). Lee C-Y; Bennett KM; Debbins JP; Choi I-Y; Lee P. The Relationship between Diffusion Heterogeneity and Microstructural Changes in High-Grade Gliomas Using Monte Carlo Simulations. Magnetic Resonance Imaging 2022, 85, 108–120. 10.1016/j.mri.2021.10.001. [PubMed: 34653578]

(33). Baron CA; Kate M; Gioia L; Butcher K; Emery D; Budde M; Beaulieu C. Reduction of Diffusion-Weighted Imaging Contrast of Acute Ischemic Stroke at Short Diffusion Times. Stroke 2015, 46 (8), 2136–2141. 10.1161/STROKEAHA.115.008815. [PubMed: 26152297]

(34). Xing S; Levesque IR A Simulation Study of Cell Size and Volume Fraction Mapping for Tissue with Two Underlying Cell Populations Using Diffusion-Weighted MRI. Magn Reson Med 2021, 86 (2), 1029–1044. 10.1002/mrm.28694. [PubMed: 33644889]

(35). Tachibana Y; Duval T; Obata T. Monte Carlo Simulator for Diffusion-Weighted Imaging Sequences. Magn Reson Med Sci 2021, 20 (2), 222–226. 10.2463/mrms.bc.2020-0013. [PubMed: 32418924]

(36). Gardier R; Villarreal Haro JL; Canales-Rodríguez EJ; Jelescu IO; Girard G; Rafael-Patiño J; Thiran J-P Cellular Exchange Imaging (CEXI): Evaluation of a Diffusion Model Including Water Exchange in Cells Using Numerical Phantoms of Permeable Spheres. Magnetic Resonance in Medicine n/a (n/a). 10.1002/mrm.29720.

(37). Grussu F; Bernatowicz K; Casanova-Salas I; Castro N; Nuciforo P; Mateo J; Barba I; Perez-Lopez R. Diffusion MRI Signal Cumulants and Hepatocyte Microstructure at Fixed Diffusion Time: Insights from Simulations, 9.4T Imaging, and Histology. Magnetic Resonance in Medicine 2022, 88 (1), 365–379. 10.1002/mrm.29174. [PubMed: 35181943]

(38). Budde MD; Frank JA Neurite Beading Is Sufficient to Decrease the Apparent Diffusion Coefficient after Ischemic Stroke. Proc Natl Acad Sci U S A 2010, 107 (32), 14472–14477. 10.1073/pnas.1004841107. [PubMed: 20660718]

(39). Li H; Jiang X; Xie J; McIntyre JO; Gore JC; Xu J. Time-Dependent Influence of Cell Membrane Permeability on MR Diffusion Measurements. Magn Reson Med 2016, 75 (5), 1927–1934. 10.1002/mrm.25724. [PubMed: 26096552]

(40). Farinas J; Kneen M; Moore M; Verkman AS Plasma Membrane Water Permeability of Cultured Cells and Epithelia Measured by Light Microscopy with Spatial Filtering. J Gen Physiol 1997, 110 (3), 283–296. 10.1085/jgp.110.3.283. [PubMed: 9276754]

(41). Zhu F; Tajkhorshid E; Schulten K. Theory and Simulation of Water Permeation in Aquaporin-1. Biophys J 2004, 86 (1), 50–57. [PubMed: 14695248]

(42). Dannhauser D; Rossi D; De Gregorio V; Netti PA; Terrazzano G; Causa F. Single Cell Classification of Macrophage Subtypes by Label-Free Cell Signatures and Machine Learning. Royal Society Open Science 2022, 9 (9), 220270. 10.1098/rsos.220270.

(43). Anderson AW; Xie J; Pizzonia J; Bronen RA; Spencer DD; Gore JC Effects of Cell Volume Fraction Changes on Apparent Diffusion in Human Cells. Magnetic Resonance Imaging 2000, 18 (6), 689–695. 10.1016/S0730-725X(00)00147-8. [PubMed: 10930778]

(44). Egeland TAM; Gaustad J-V; Galappathi K; Rofstad EK Magnetic Resonance Imaging of Tumor Necrosis. Acta Oncologica 2011, 50 (3), 427–434. 10.3109/0284186X.2010.526633. [PubMed: 20950229]

(45). Fukukura Y; Kumagae Y; Fujisaki Y; Nakamura S; Dominik Nickel M; Imai H; Yoshiura T. Extracellular Volume Fraction with MRI: As an Alternative Predictive Biomarker to Dynamic Contrast-Enhanced MRI for Chemotherapy Response of Pancreatic Ductal Adenocarcinoma. European Journal of Radiology 2021, 145, 110036. 10.1016/j.ejrad.2021.110036.

(46). Li M; Liu Z; Wu Y; Zheng N; Liu X; Cai A; Zheng D; Zhu J; Wu J; Xu L; Li X; Zhu L-Q; Manyande A; Xu F; Wang J. In Vivo Imaging of Astrocytes in the Whole Brain with Engineered AAVs and Diffusion-Weighted Magnetic Resonance Imaging. Mol Psychiatry 2022, 1–8. 10.1038/s41380-022-01580-0.

(47). Zhang L; Gong M; Lei S; Cui C; Liu Y; Xiao S; Kang X; Sun T; Xu Z; Zhou C; Zhang S; Zhang D. Targeting Visualization of Malignant Tumor Based on the Alteration of DWI Signal Generated by HTERT Promoter–Driven AQP1 Overexpression. Eur J Nucl Med Mol Imaging 2022, 49 (7), 2310–2322. 10.1007/s00259-022-05684-1. [PubMed: 35044495]

(48). Zheng N; Li M; Wu Y; Kaewborisuth C; Li Z; Gui Z; Wu J; Cai A; Lin K; Su K-P; Xiang H; Tian X; Manyande A; Xu F; Wang J. A Novel Technology for in Vivo Detection of Cell Type-Specific Neural Connection with AQP1-Encoding RAAV2-Retro Vector and Metal-Free MRI. NeuroImage 2022, 258, 119402. 10.1016/j.neuroimage.2022.119402.

(49). White NS; Dale AM Distinct Effects of Nuclear Volume Fraction and Cell Diameter on High B-Value Diffusion MRI Contrast in Tumors. Magn Reson Med 2014, 72 (5), 1435–1443. 10.1002/mrm.25039. [PubMed: 24357182]

(50). Lee H-H; Fieremans E; Novikov DS Realistic Microstructure Simulator (RMS): Monte Carlo Simulations of Diffusion in Three-Dimensional Cell Segmentations of Microscopy Images. J Neurosci Methods 2021, 350, 109018. 10.1016/j.jneumeth.2020.109018.

(51). Johnson GA; Tian Y; Ashbrook DG; Cofer GP; Cook JJ; Gee JC; Hall A; Hornburg K; Qi Y; Yeh F-C; Wang N; White LE; Williams RW Merged Magnetic Resonance and Light Sheet Microscopy of the Whole Mouse Brain. Proceedings of the National Academy of Sciences 2023, 120 (17), e2218617120. 10.1073/pnas.2218617120.

(52). Caruyer E; Lenglet C; Sapiro G; Deriche R. Design of Multishell Sampling Schemes with Uniform Coverage in Diffusion MRI. Magn Reson Med 2013, 69 (6), 1534–1540. 10.1002/mrm.24736. [PubMed: 23625329]

(53). Nedjati-Gilani GL; Schneider T; Hall MG; Cawley N; Hill I; Ciccarelli O; Drobnjak I; Wheeler-Kingshott CAMG; Alexander DC Machine Learning Based Compartment Models with Permeability for White Matter Microstructure Imaging. NeuroImage 2017, 150, 119–135. 10.1016/j.neuroimage.2017.02.013. [PubMed: 28188915]

(54). Palombo M; Ligneul C; Najac C; Le Douce J; Flament J; Escartin C; Hantraye P; Brouillet E; Bonvento G; Valette J. New Paradigm to Assess Brain Cell Morphology by Diffusion-Weighted MR Spectroscopy in Vivo. Proceedings of the National Academy of Sciences 2016, 113 (24), 6671–6676. 10.1073/pnas.1504327113.

(55). Rensonnet G; Scherrer B; Girard G; Jankovski A; Warfield SK; Macq B; Thiran J-P; Taquet M. Towards Microstructure Fingerprinting: Estimation of Tissue Properties from a Dictionary of Monte Carlo Diffusion MRI Simulations. NeuroImage 2019, 184, 964–980. 10.1016/j.neuroimage.2018.09.076. [PubMed: 30282007]

(56). Nilsson M; Alerstam E; Wirestam R; Ståhlberg, F.; Brockstedt, S.; Lätt, J. Evaluating the Accuracy and Precision of a Two-Compartment Kärger Model Using Monte Carlo Simulations. Journal of Magnetic Resonance 2010, 206 (1), 59–67. 10.1016/j.jmr.2010.06.002. [PubMed: 20594881]

(57). Zhang RB; Verkman AS Water and Urea Permeability Properties of Xenopus Oocytes: Expression of MRNA from Toad Urinary Bladder. Am J Physiol 1991, 260 (1 Pt 1), C26–34. 10.1152/ajpcell.1991.260.1.C26. [PubMed: 1987778]

(58). Han Y; Liu X-M; Liu H; Li S-C; Wu B-C; Ye L-L; Wang Q-W; Chen Z-L Cultivation of Recombinant Chinese Hamster Ovary Cells Grown as Suspended Aggregates in Stirred Vessels. Journal of Bioscience and Bioengineering 2006, 102 (5), 430–435. 10.1263/jbb.102.430. [PubMed: 17189170]

(59). Voos P; Fuck S; Weipert F; Babel L; Tandl D; Meckel T; Hehlgans S; Fournier C; Moroni A; Rödel F; Thiel G. Ionizing Radiation Induces Morphological Changes and Immunological Modulation of Jurkat Cells. Frontiers in Immunology 2018, 9.

(60). Ross PE; Garber SS; Cahalan MD Membrane Chloride Conductance and Capacitance in Jurkat T Lymphocytes during Osmotic Swelling. Biophys J 1994, 66 (1), 169–178. 10.1016/S0006-3495(94)80754-4. [PubMed: 8130336]

(61). Skoge M; Donev A; Stillinger FH; Torquato S. Packing Hyperspheres in High-Dimensional Euclidean Spaces. Phys. Rev. E 2006, 74 (4), 041127. 10.1103/PhysRevE.74.041127.

(62). Jelescu IO; Grussu F; Ianus A; Hansen B; Barrett RLC; Aggarwal M; Michielse S; Nasrallah F; Syeda W; Wang N; Veraart J; Roebroeck A; Bagdasarian AF; Eichner C; Sepehrband F; Zimmermann J; Soustelle L; Bowman C; Tendler BC; Hertanu A; Jeurissen B; Verhoye M; Frydman L; van de Looij Y; Hike D; Dunn JF; Miller K; Landman BA; Shemesh N; Anderson A; McKinnon E; Farquharson S; Acqua FD; Pierpaoli C; Drobnjak I; Leemans A; Harkins KD; Descoteaux M; Xu D; Huang H; Santin MD; Grant SC; Obenaus A; Kim GS; Wu D; Bihan DL; Blackband SJ; Ciobanu L; Fieremans E; Bai R; Leergaard T; Zhang J; Dyrby TB; Johnson GA;

Cohen-Adad J; Budde MD; Schilling KG Recommendations and Guidelines from the ISMRM Diffusion Study Group for Preclinical Diffusion MRI: Part 1 -- In Vivo Small-Animal Imaging. arXiv April 21, 2023. 10.48550/arXiv.2209.12994.

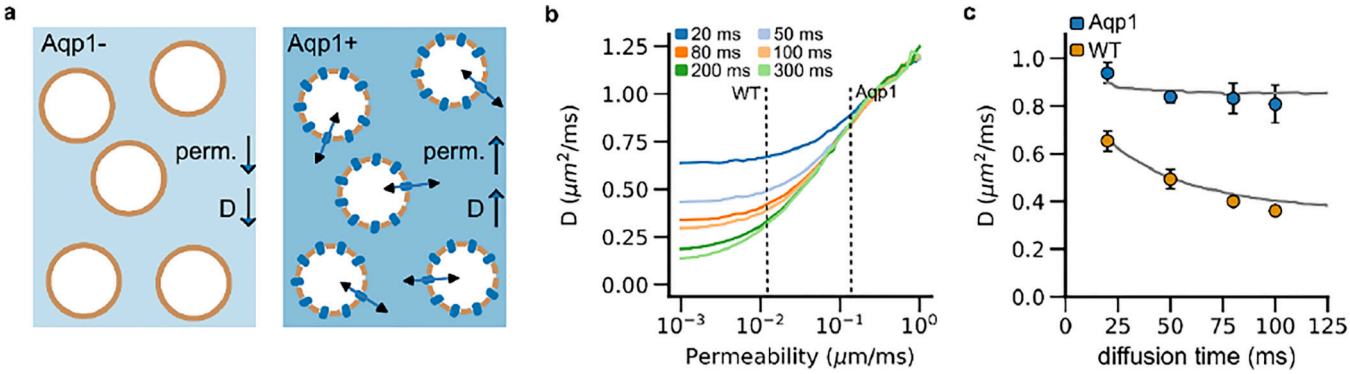

Figure 1: Monte Carlo simulations of water diffusion in cells with varying plasma membrane permeability.

a, Engineering cells to express Aqp1 makes their membrane more permeable to water molecules than wild-type (viz. non-engineered) cells. **b**, Molecular diffusivity (D) increases with membrane permeability. Longer diffusion times lead to a decrease in diffusivity as a larger number of water molecules encounter the plasma membrane, which restricts free movement of water molecules. The dashed vertical lines correspond to permeability coefficients of wild-type (WT) and Aqp1-expressing CHO cells. **c**, Diffusivity decreases more markedly with diffusion time in wild-type cells (less permeable) than in cells engineered to express Aqp1 (more permeable). Therefore, long diffusion times are ideal for maximizing the Aqp1-driven fold change in diffusivity. However, given the diminishing SNR at long diffusion times, we used $100\ ms$ to achieve an optimal trade-off between the fold change in diffusivity and SNR. The solid lines represent the simulated diffusivities for a synthetic substrate consisting of spherical cells of radius $7.6\ \mu m$ packed to yield a total intracellular volume fraction of 0.65. Wild-type and Aqp1-expressing cells were modeled using permeability coefficients of 0.012 and 0.138 $\mu m/ms$, respectively. Circles denote experimental data obtained from pellets of CHO cells at 7 T. Error bars represent the standard deviation ($n \geq 5$ biological replicates).

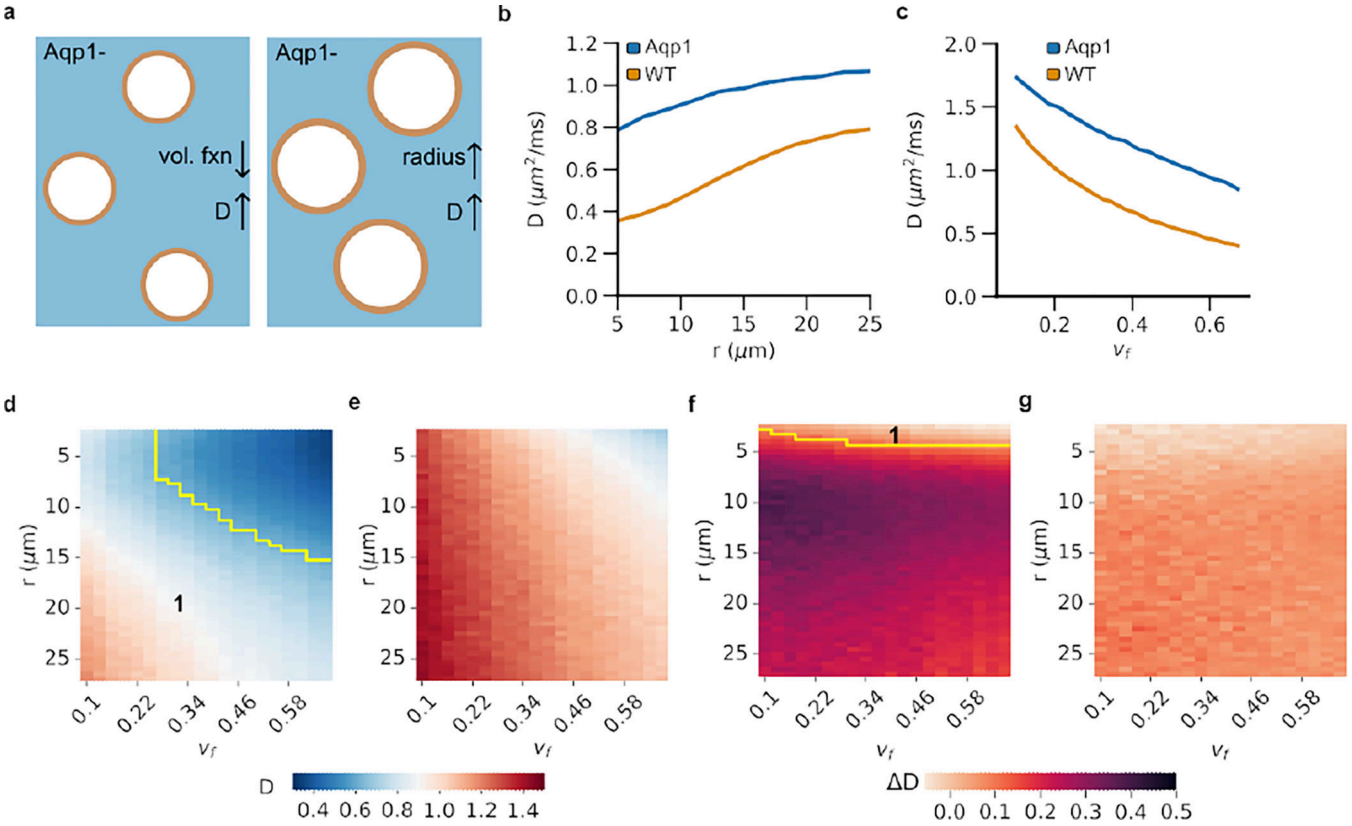

Figure 2: Effect of cell size and intracellular volume fraction on diffusivity.

a, Changes in tissue microstructure, such as reduced intracellular volume fraction (v_f) or larger cell radius (r), can increase diffusivity (D) similar to Aqp1 expression. **b**, Simulated diffusivity at 100 ms for a fixed volume fraction ($v_f = 0.65$) increases with cell radius in both Aqp1-expressing and wild-type cells, but Aqp1 expression reduces the size dependence of diffusivity. **c**, Simulated diffusivity (100 ms) for a given cell size ($r = 7.6$ μm) shows an inverse correlation with intracellular volume fraction in Aqp1-expressing and wild-type cells. **d**, Heatmap showing the combined dependence of diffusivity (100 ms) on cell size and intracellular volume fraction in wild-type and **e**, Aqp1-expressing cells. In the region marked as 1, Aqp1 signals are difficult to distinguish from the tissue background because wild-type diffusivities fall within the same range of diffusivities observed in Aqp1-expressing cells. **f**, Heatmap showing the dependence of differential diffusivity, viz. $\Delta D = D_{20\ ms} - D_{100\ ms}$, on cell size and intracellular volume fraction in wild-type and **g**, Aqp1-expressing cells. The ΔD metric significantly reduces the overlap (region of overlap marked as **1** in the heatmap) between cell populations expressing Aqp1 and wild-type cells, thereby providing a reliable readout of Aqp1 expression that is unaffected by tissue microstructure parameters. The color-bars represent molecular diffusivity of water (D) or differential diffusivity (ΔD) in units of um^2/ms. Wild-type and Aqp1-expressing cells were modeled with permeability coefficients of 0.012 and 0.138 $\mu m/ms$, respectively.

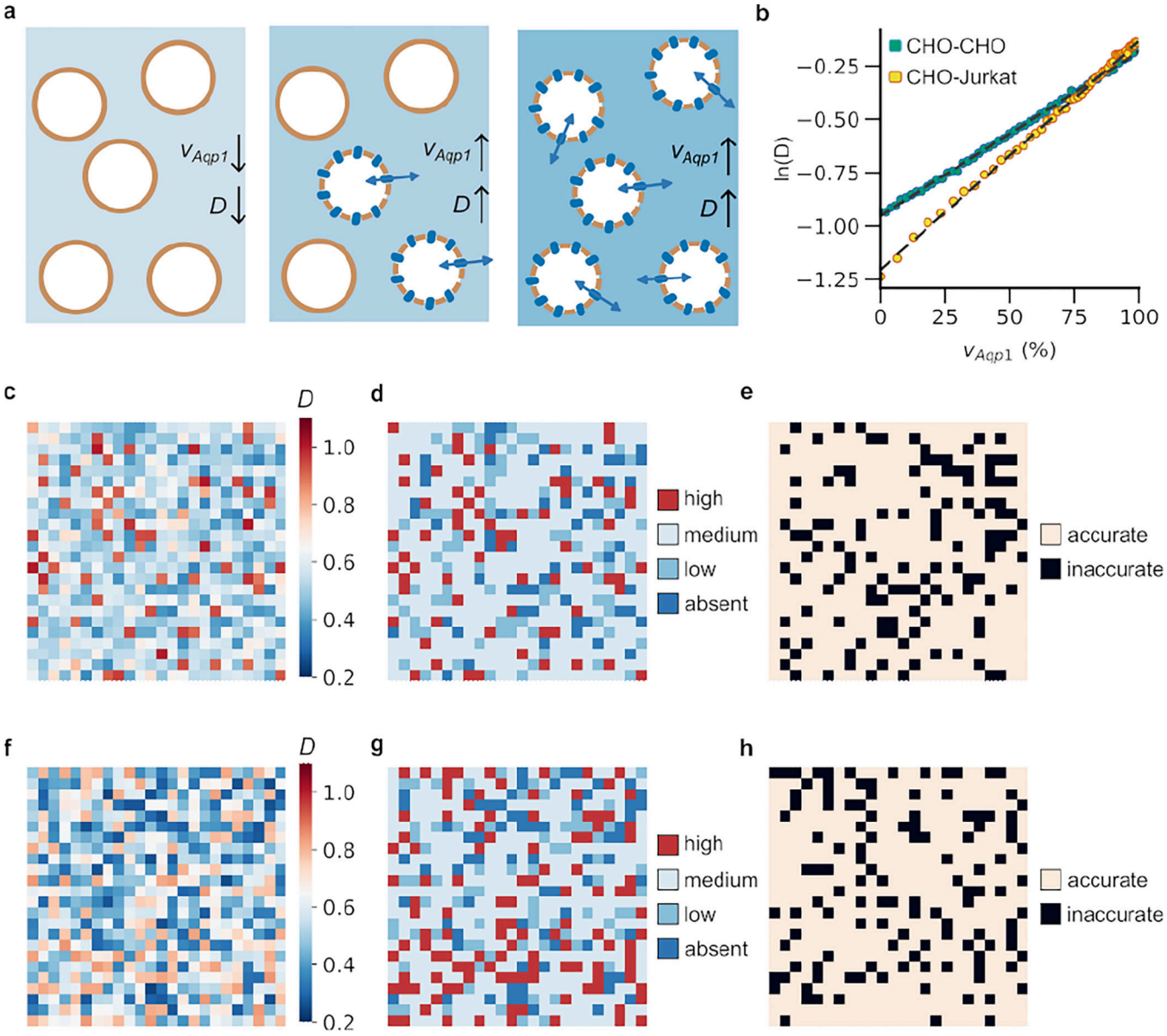

Figure 3: Imaging of mixed-cell populations using Aqp1.

a, Diffusivity (D) of a mixed-cell population increases when more Aqp1-expressing cells are present. **b**, The relationship between diffusivity and volume fraction of Aqp1-expressing cells (v_{Aqp1}) can be modeled by a log-linear function for mixed populations containing Aqp1-expressing CHO cells and either wild-type CHO or wild-type Jurkat cells. **c**, A representative example of a 24 × 24 pixel mixed-cell mosaic created using randomly chosen pixels from experimental diffusion maps of cell populations comprising varying fractions of CHO-Aqp1 cells mixed with wild-type CHO cells. Each pixel in the image corresponds to an experimentally determined diffusion coefficient. **d**, The mapping between diffusivity and v_{Aqp1} is used to distinguish pixels into one of four levels reflecting the volume percentage of Aqp1-expression: absent ($v_{Aqp1} < 10\ \%$), low ($10\ \% \leq\ v_{Aqp1} < 30\ \%$), medium ($30\ \% \leq\ v_{Aqp1} \leq 70\ \%$), and high ($v_{Aqp1} > 70\ \%$). **e**, Pixels that are classified correctly are

shown in a lighter shade, whereas those that are classified incorrectly are shown in black. **f**, Representative example of a 24 × 24 pixel mixed-cell mosaic created from diffusion maps of mixed populations comprising varying fractions of CHO-Aqp1 cells mixed with wild-type Jurkat cells. **g**, Each pixel was classified into one of four levels, reflecting the volume percentage of Aqp1-expressing cells. **h**, Correctly classified pixels are shown in a lighter shade, whereas those that are classified incorrectly are shown in black. The color-bars in **c** and **f** represent diffusivity in $\mu m^2/ms$. All diffusivity values correspond to a diffusion time of 100 ms.

Table 1:

Voxel-wise classification of Aqp1 volume fraction in mixed-cell populations comprising Aqp1-expressing and wild-type CHO cells. Error represents the standard deviation from applying the log-linear classification model on $n = 100$ mixed-cell images constructed by randomly sampling voxels from experimental diffusion maps.

Aqp1-level	Specificity	Recall	Precision
Absent (< 10 %)	0.953 ± 0.005	0.529 ± 0.040	0.583 ± 0.031
Low ($10 - 30$ %)	0.935 ± 0.006	0.383 ± 0.027	0.626 ± 0.028
Medium ($30 - 70$ %)	0.759 ± 0.014	0.975 ± 0.005	0.835 ± 0.008
High (> 70 %)	0.996 ± 0.002	1.0	0.967 ± 0.017

Table 2:

Voxel-wise classification of Aqp1 volume fraction in mixed-cell populations comprising Aqp1-expressingCHO cells mixed with wild-type Jurkat cells. Error represents the standard deviation from applying the log-linear classification model on $n = 100$ mixed-cell images constructed by randomly sampling voxels from experimental diffusion maps.

Aqp1-level	Specificity	Recall	Precision
Absent (< 10 %)	0.973 ± 0.003	0.885 ± 0.028	0.806 ± 0.017
Low ($10 - 30$ %)	0.984 ± 0.004	0.504 ± 0.020	0.898 ± 0.022
Medium ($30 - 70$ %)	0.805 ± 0.010	0.828 ± 0.006	0.842 ± 0.007
High (> 70 %)	0.892 ± 0.004	1.0	0.538 ± 0.009